PAPER

Check for updates

Metal oxide cluster-integrated polymer networks for robust solid-state single-ion conduction at high temperatures†

Jie Deng, Litao Ma, Lu Liu, Weigang Sun, Yuan Liu and Panchao Yin 🔟 *

Ion conduction at high temperatures is critical for the improvement of working efficiency and stability of energy-conversion and -storage devices. Ceramics and highly rigid polymers are generally applied for achieving this; however, their poor processability and mechanical properties hinder their extensive applications. Herein, a sub-nanometer anionic metal oxide cluster ($\{V_6O_{13}[(OCH_2)_3CR]_2\}^{2-}$) was covalently integrated into polymer networks for high-temperature solid-state conduction of H^+ and Li^+ single-ion electrolytes. The hexavanadate cluster was functionalized with acrylate groups, and it served as a nano-scale bifunctional crosslinker to copolymerize with poly(ethylene glycol) methacrylate for the fabrication of polymer networks. The associated counter-cations of the immobilized hexavanadate could be fully solvated in the melts of poly(ethylene glycol) for realizing high mobilities, contributing to promising single-ion conductivities and achieving an Li^+ transference number of 0.84. According to dielectric spectroscopy studies, the transport of Li^+ ions was directly mediated by side chain dynamics. The counter-cations could be feasibly switched for the conduction of various cations, such as H^+ and Li^+. Meanwhile, the covalent and supramolecular interactions between the polymer and inorganic hexavanadate afforded enhanced stability and robust ionic conduction at temperatures as high as 200 °C. Thus, this work provides versatile platform chemical systems for robust solid-state single-ion conduction at high temperatures.

Introduction

The rapid growth of the energy industry imposes high expectations on the energy density, stability and safety of energy storage and conversion devices.[1–3] Accordingly, one of the top research priorities is the development of solid-state electrolytes (SSEs) with promising ionic conductivities while overcoming the issues of leaking, dendrite initiation and interfacial instability.[4–14] Typically, the proton exchange membranes (PEMs) in fuel cells (FCs), SSEs in lithium-ion batteries (LIBs) and supercapacitors are under intense research for achieving optimized and robust performance of energy devices.[14–22] Meanwhile, the LIB industry desires single-ion conduction of SSEs as the accumulation of anions at the anode causes strong polarization and reduces the operating voltage of the battery.[20,23] To further enhance efficiency and safety, SSEs that can function at high temperatures are highly desired.[24] They can extend the application of LIBs at high temperature conditions and ensure their safety even at short-circuit conditions.[25,26] For FCs, the PEMs that stably work at temperatures above 100 °C can significantly enhance the efficiency of catalysts and reduce the poisoning of noble metal catalysts by the impurities in H_2 gas.[27–29] Inorganic electrolytes such as ceramics have been applied for high temperature single-ion SSEs; nevertheless, their poor processability and high interfacial impedance with electrode materials limit their applications, especially in mobile and portable devices.[30–32] The hybridization of inorganic electrolytes with polymers offers great potential to realizing ideal SSEs with comprehensive advantages in ion conduction, processability, flexibility and stability at extreme conditions.[13,33–36] However, achieving a synergistic effect is still challenging, and only a few examples have been reported owing to the lack of an effective protocol to rationally and precisely tune the interaction between polymers and inorganics.[37]

Metal oxide clusters (MOCs) are a group of precisely defined, mono-dispersed inorganic nanoparticles (NPs) with sizes ranging from sub-nanometer to *ca.* 10 nm.[38] Their surface structures can be feasibly tailored, and they exhibit a broad range of interactions with polymers, ranging from covalent bonding to various supramolecular interactions.[39–44]

State Key Laboratory of Luminescent Materials and Devices & South China Advanced Institute for Soft Matter Science and Technology, Guangdong Basic Research Center of Excellence for Energy & Information Polymer Materials, South China University of Technology, Guangzhou 510641, P. R. China. E-mail: yinpc@scut.edu.cn

© 2025 The Author(s). Published by the Royal Society of Chemistry

RSC Appl. Polym., 2025, **3**, 1177–1182 | **1177**

Some MOCs, such as polyoxometalates (POMs), possess certain amounts of negative charges, and the associated counterions can be applied as mobile cations for electrolytes.[37,45,46] Herein, a sub-nanometer anionic hexavanadate ($\{V_6O_{13}[(OCH_2)_3CR]_2\}^{2-}$, abbreviation V_6) was functionalized with acrylate groups, and it further copolymerized with poly (ethylene glycol) methacrylate (PEGMA) for the fabrication of polymer networks. The counter-cations could be feasibly switched for the conduction of various cations, such as H^+ and Li^+. Their ionic conduction was evaluated for single-ion conduction and high temperature stability performance. The microscopic mechanism of ion transport was probed using broadband dielectric spectroscopy for understanding the structure–property relationship.

Experimental

Materials and synthesis

The purchased PEGMA with an average molecular weight (M_w) of 360 g mol^{-1} was filtered through an alkaline alumina column to remove the polymerization inhibitor and was used directly in the synthetic protocol for fabricating polymer metal–oxygen cluster electrolyte (PMCE) nanocomposites. Initially, PEGMA, methacrylic anhydride-modified hexavanadates (MAHVs), and the initiator potassium persulfate (KPS) were dissolved in deionized water. Subsequently, the mixed solution was transferred into a glass mold with a thickness of 1 mm. The mold was then sealed and placed in an oven that was pre-heated to 70 °C for 24 h (keeping an anaerobic environment throughout the process). Detailed descriptions of the covalent modification process of MAHVs and their covalent polymerization with PEGMA are provided in the ESI.†

Measurements

Prior to all measurements, the samples were dried in a vacuum oven at room temperature for two weeks to remove water content. Small-angle X-ray scattering (SAXS) data were collected at the beamline BL16B1 of the Shanghai Synchrotron Radiation Facility (SSRF) using a Pilatus 2M detector. Wide-angle X-ray scattering (WAXS) data were collected using a two-dimensional wide-angle X-ray diffraction instrument equipped with the HomeLab system of Rigaku. The resulting samples were dissolved in deuterated reagent, and tetramethylsilane (TMS) was selected as the internal reference. NMR data were recorded on a BRUKER AVANCE 500 instrument at 25 °C. FT-IR spectra were measured in the range of 600–4000 cm^{-1} using the attenuated total reflectance (ATR) mode of a PerkinElmer. All the tests were performed in an N_2 atmosphere. Thermogravimetric analysis (TGA) was performed using a TA TGA 5500 equipment within a temperature range of 30 °C to 600 °C at a heating rate of 10 °C min^{-1} in an air atmosphere. Differential scanning calorimetry (DSC) tests were carried out on a DSC 2500 instrument from TA instruments at a heating rate of 10 °C min^{-1} in a nitrogen atmosphere. The temperature range was −80 °C to 100 °C for the LiPMCEs. Viscoelastic pro-

perties of the LiPMCE nanocomposites were studied using an Anton Paar Rheometer 302 (MCR 302) equipped with an 8 mm diameter cone plate from 30 °C to 100 °C. Alternating current (AC) impedance measurements were carried out on a CHI660E electrochemical workstation with two parallel copper plate electrodes over 10^{-1} Hz to 10^6 Hz ranging from 40 °C to 100 °C in an oven. The ion conductivity of the membranes was calculated using the following equation:

$$\sigma = \frac{L}{AR_b} \tag{1}$$

where R_b is obtained by the intercept of the Nyquist plot with the real axis, A is the area of the copper sheet electrodes, and L is the distance between the two electrodes (i.e., thickness of the membrane). The BDS measurements were carried out using a Novocontrol Concept 80 system with an Alpha-ANB impedance analyzer and a Quatro Cryosystem temperature system. The electrode polarization was avoided by isolating the metallic electrodes with a thin Teflon film. The HN relaxation frequency was obtained by fitting the dielectric loss peak with the Havriliak–Negami (HN) equation,

$$\varepsilon''(f) = -\mathcal{J}\left[\frac{\Delta\varepsilon}{(1 + (if/f_{HN})^m)^n}\right] \tag{2}$$

where f_{HN} and $\Delta\varepsilon$ are the HN relaxation frequency and dielectric strength of each dielectric loss peak, respectively, and m and n are used to describe the asymmetry of the dielectric loss peaks.

Results and discussion

Molecular design and structural characterization

The copolymerization strategy was applied to ensure the stability of SSEs and the feasibility of SSE fabrication and cation replacement (Fig. 1). The selected V_6 cluster possesses a super-octahedron topology with a particle size of ∼0.8 nm. Owing to the well-developed chemistry of V_6 cluster, its surface was precisely and covalently functionalized with two acrylate groups for further polymerization (Fig. S2†). Meanwhile, the V_6 cluster carried two negative charges, and its counter-cations could be feasibly tuned for investigating the conduction of different ions. The typical radical polymerization of the bi-functionalized V_6 monomer with PEGMA afforded polymer networks with tunable flexibility, which was defined by the content of the V_6 crosslinker (Fig. S3†).

The structural analysis from SAXS studies suggested consistent polymer packing between the hybrid network and PEGMA monomers based on their similar scattering patterns from 0.8–1.8 Å^{-1}. The side chains of the PEGMA units formed a matrix of low-M_w PEG melt in the framework, which facilitated diffusion of the counter-cations (e.g., H^+ and Li^+) of V_6. Meanwhile, the characteristic form factor of V_6 cluster was observed at 1.5–3.6 Å^{-1} region after subtracting the contribution of the polymers, indicating the intact of V_6 structures in the hybrid framework (Fig. 2a). More evidence for the suc-
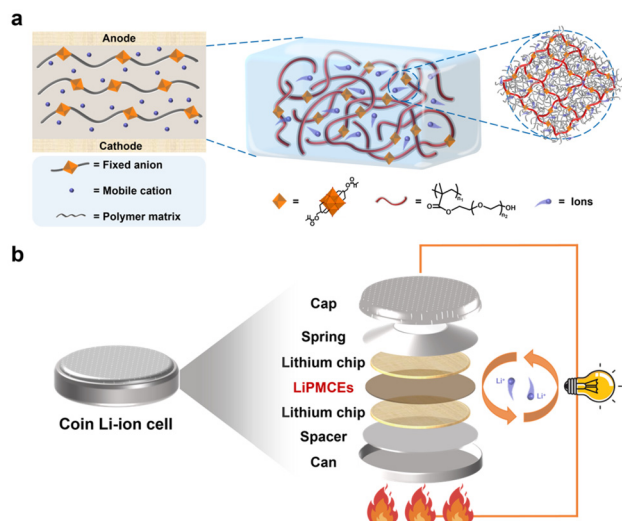
Fig. 1 (a) Schematic of the microstructure of the PMCEs, and counter-cation transfer mechanism by side chains. (b) Schematic of the 0.16% LiPMCEs assembled into a coin cell structure that can be used under high-temperature conditions.
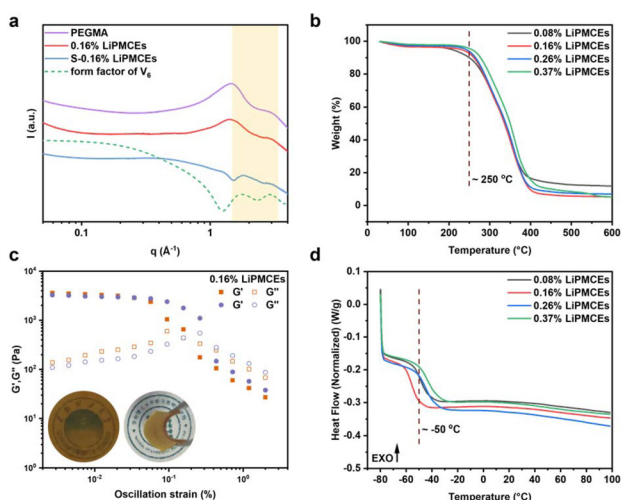

Fig. 2 Microstructure and macroscopic properties of PMCEs. (a) SAXS/WAXS curves of PEGMA, 0.16% LiPMCEs and S-0.16% LiPMCEs (Using PEGMA as background, the structural information of V_6 was obtained after subtracting the background from the scattering signal of LiPMCEs.) at RT. (b) TGA curves of LiPMCEs (0.08%, 0.16%, 0.26%, and 0.37 wt%). (c) 0.16% LiPMCEs subjected to two consecutive amplitude sweeps (both at 150 °C) to evaluate their flexibility; the inset figures show 0.16% LiPMCE nanocomposites. (d) DSC curves of LiPMCEs (0.08%, 0.16%, 0.26%, and 0.37 wt%).

interaction between V_6 and PEG and the nano-reinforcing effect of V_6 contributed to the increased mechanical strength (Fig. S5†). The flexibility of the hybrid networks with 0.08%–0.37 wt% loadings of V_6 could be maintained at strains higher than 200% in shear tests (Fig. 2c). The covalent networks facilitated stable mechanical strength at high temperature ranges, enabling their application as high-temperature SSEs (Fig. S6†). Meanwhile, the glass transition temperatures (T_gs) (Fig. 2d) of the PEG segments remained in the low-temperature range (~-50 °C) for the networks, suggesting that the fast segment dynamics of PEG was maintained for effective ion transportation.

High-temperature single-ion conduction

The hybrid networks could be feasibly switched for the conduction of various cations by simply replacing the counter-cations of V_6. The conduction of H^+ and Li^+ was studied as typical examples for their critical applications as SSEs in fuel cells and LIBs. All the obtained HPMCEs with different V_6 loadings exhibited high proton conductivities, among which the V_6 clusters in 0.08% HPMCEs provided the highest concentration of protons. Their dispersion in polymer PEG substrates remained excellent, achieving the highest conductivity of 4.77×10^{-6} S cm^{-1} at 200 °C (Fig. 3a). Currently, the operational temperature of high-temperature proton fuel cells is predominantly confined to approximately 160 °C.[47–49] Here, the synergistic covalent and supramolecular interactions between PEG and V_6 substantially reinforced the structural integrity of the cross-linked network. Consequently, HPMCEs achieved exceptional proton conduction stability, sustaining reliable performance at temperatures as high as 200 °C.
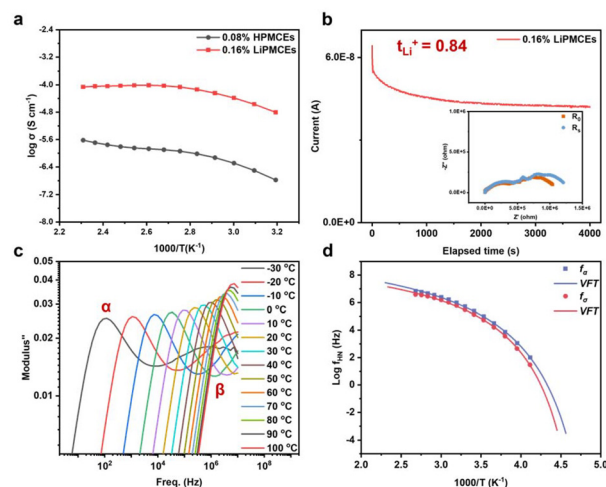

Fig. 3 Kinetic behavior and electrochemical properties of PMCEs (a) Ionic conductivity as a function of temperature from 40 °C to 160 °C with 10 °C intervals. (b) Polarization of the Li|0.16% LiPMCEs|Li cell at an applied voltage of 10 mV; inset: Nyquist plots of the Li|0.16% LiPMCEs|Li cell before and after polarization. (c) Modulus loss spectra of 0.16% LiPMCEs from −30 to 100 °C, with the α and β relaxation peaks in the figure corresponding to −30 °C. (d) Temperature-dependence of structure (τ_α) and conductivity (τ_σ) relaxation times in 0.16% LiPMCEs.

cessful incorporation of V_6 into the network was provided by the FT-IR spectrum (Fig. S4a†). Thermal analysis confirmed the high stability of LiPMCEs up to 250 °C, indicating their application in high-temperature ion conductors (Fig. 2b).

The mechanical properties and processabilities of SSEs are critical for their application in portable devices, especially in flexible batteries and supercapacitors. The supramolecular

© 2025 The Author(s). Published by the Royal Society of Chemistry

RSC Appl. Polym., 2025, **3**, 1177–1182 | **1179**

Building on the excellent high-temperature performance of HPMCEs, to extend the high-temperature application of LIBs, LiPMCEs were developed by replacing the counterions in V_6 clusters with Li^+. The lithium-ion conductivity of LiPMCEs was systematically investigated, which revealed a strong dependence on V_6 cluster loading. At a loading of 0.16%, the V_6 clusters were uniformly dispersed in the PEG matrix, providing sufficient Li^+ concentration and achieving an optimal cross-linking density while avoiding ion channel blockage caused by excessive aggregation. The 0.16% LiPMCEs exhibited a room-temperature (30 °C) conductivity of 8.38×10^{-6} S cm^{-1}, surpassing those of traditional SSEs (typically 10^{-7}–10^{-6} S cm^{-1}). Moreover, while conventional SSEs are generally limited to temperatures below 80 °C,[50] LiPMCEs demonstrated remarkable thermal stability and stable conductivity even at 200 °C. At 110 °C, the conductivity reached 9.69×10^{-5} S cm^{-1}, showcasing excellent high-temperature ion transport properties. This stability was attributed to the strong interactions between PEG and V_6 clusters, which preserved the structural integrity of the network at elevated temperatures, preventing electrolyte decomposition or ion channel collapse. These results highlight the potential of LiPMCEs as advanced SSEs for high-temperature LIB applications, simultaneously achieving superior conductivity and thermal stability. Further optimization of V_6 loading and exploration of electrode compatibility could advance their practical use in next-generation energy storage systems. The formation of an ordered structure with ion channels provided excellent ionic conductivity and a high Li^+ transference number. Using the potentiodynamic polarization method, 0.16% LiPMCEs were tested at room temperature, with chronoamperometry profiles and EIS spectra (before and after polarization) shown in Fig. 3b. The Li^+ transference number (t_{Li^+}) was calculated to be 0.84 (averaged) using the following equation,

$$t_{Li^+} = \frac{I_s(\Delta V - I_0 R_0)}{I_0(\Delta V - I_s R_s)} \qquad (3)$$

which was consistent with previously reported single-ion SSEs. In our SSEs, cations migrated through PEG-based ion channels while immobile anions served as cross-linkers, enabling single-ion conduction.

Structural relaxation dynamics and microscopic mechanisms

To elucidate the microscopic mechanism of ion transport in LiPMCEs, BDS was employed to quantify the correlation between ion transport and structural relaxation dynamics. In the DC conductivity (σ_{dc}) spectra (Fig. S8a†), a low-frequency σ_{dc} plateau represented long-range ion diffusion, while a power-law frequency dependence ($\sigma' \sim \omega^n$) in the high-frequency region indicated short-range sub-diffusive ion motion. The crossover frequency (ν) between these regimes reflected the transition from sub-diffusive to diffusive motion and served as a measure of ion mobility. Both the conductivity relaxation time ($\tau_\sigma = \nu^{-1}$) and σ_{dc} were derived from the random barrier model (RBM) fitting of the σ_{dc} spectra

(Fig. S8b†). Additionally, the structural relaxation time (τ_α), obtained by fitting the dielectric loss modulus (M'') with the Havriliak–Negami (HN) function, characterized the structural dynamics of the SSEs (Fig. S9†).

In the BDS studies of 0.16% LiPMCEs, two structural relaxation processes were observed at lower temperatures (<253 K), corresponding to the slow motion of the PEG chain segment (α) and fast dynamics originating from the secondary relaxation of PEG (β) in the dielectric loss modulus spectra. As the temperature increased, the β relaxation process of LiPMCEs was accelerated and eventually slipped out of the test frequency range, while the α relaxation process at relatively low frequencies showed a steady movement toward higher frequencies (Fig. 3c). Interestingly, τ_α and τ_σ were similar and followed the same relaxation mechanism, $i.e.$, they followed the Vogel–Fulcher–Tammann (VFT) temperature dependence (Fig. 3d), which suggested that the ion transport dynamics were closely linked to the chain segment dynamics in this system. The conducting cations maintained strong interactions with the PEG chain segments. This finally contributed to the improvement of cation conductivity and VFT temperature dependence of ionic conductivities.

Conclusions

In summary, we proposed a single-ion conductive composite system capable of stable ion transport under high-temperature conditions. This system was obtained via the covalent cross-linking of counterion-tunable inorganic nanoparticles with polymers, resulting in an SSE that exhibited notable flexibility and good processability. The design, which incorporated both covalent and supramolecular interactions, significantly enhanced the environmental stability and safety of the SSE. BDS analysis demonstrated that the polymer network, featuring continuous ion channels formed via the covalent polymerization of organic components and MOCs, facilitated ion transport through polymer chain segment motion, thereby optimizing the conductive properties of the material. Owing to the feasible surface modifications of MOCs and the broad selection of counterions, the hybrid SSE provided a versatile platform for functional electrolytes. This research offers new opportunities for the fabrication of ion exchange membranes for high-temperature hydrogen fuel cells and lithium batteries under extreme working conditions.

Author contributions

Jie Deng: conceptualization, data curation, formal analysis, investigation, methodology, validation, writing – original draft. Litao Ma: investigation, methodology, formal analysis. Lu Liu: formal analysis, visualization. Weigang Sun: formal analysis. Yuan Liu: visualization. Panchao Yin: conceptualization, data curation, supervision, project administration, funding acquisition, writing – review & editing.

Conflicts of interest

There are no conflicts to declare.

Data availability

The data supporting this article have been included as part of the ESI.†

The NMR, FT-IR, TGA, DSC, ICP-OES, SAXS, WAXS, AC, BDS, and rheological data supporting this study's findings are provided within the manuscript and ESI.†

Acknowledgements

References

1 L. Yue, J. Ma, J. Zhang, J. Zhao, S. Dong, Z. Liu, G. Cui and L. Chen, *Energy Storage Mater.*, 2016, **5**, 139–164.

2 L. Houston, D. J. Heldebrant, E. Fox, D. A. Cullen, O. K. Farha and J. Liu, *ACS Appl. Mater. Interfaces*, 2022, **14**, 20303–20305.

3 J.-M. Ma and Y.-T. Li, *Rare Met.*, 2021, **40**, 246–248.

4 K. Murata, S. Izuchi and Y. Yoshihisa, *Electrochim. Acta*, 2000, **45**, 1501–1508.

5 Z. Gao, H. Sun, L. Fu, F. Ye, Y. Zhang, W. Luo and Y. Huang, *Adv. Mater.*, 2018, **30**, e1705702.

6 Y. Liu, P. He and H. Zhou, *Adv. Energy Mater.*, 2017, **8**, 1701602.

7 S. Ahmad, *Ionics*, 2009, **15**, 309–321.

8 J. Shim, D.-G. Kim, J. H. Lee, J. H. Baik and J.-C. Lee, *Polym. Chem.*, 2014, **5**, 3432–3442.

9 J. B. Goodenough and K. S. Park, *J. Am. Chem. Soc.*, 2013, **135**, 1167–1176.

10 Y. Kato, S. Hori, T. Saito, K. Suzuki, M. Hirayama, A. Mitsui, M. Yonemura, H. Iba and R. Kanno, *Nat. Energy*, 2016, **1**, 16030.

11 J. B. Goodenough and Y. Kim, *Chem. Mater.*, 2009, **22**, 587–603.

12 N. Kamaya, K. Homma, Y. Yamakawa, M. Hirayama, R. Kanno, M. Yonemura, T. Kamiyama, Y. Kato, S. Hama, K. Kawamoto and A. Mitsui, *Nat. Mater.*, 2011, **10**, 682–686.

13 T. Sun, Q. Liang, S. Wang and J. Liao, *Small*, 2024, **20**, e2308297.

14 J. Li, Y. Cai, H. Wu, Z. Yu, X. Yan, Q. Zhang, T. Z. Gao, K. Liu, X. Jia and Z. Bao, *Adv. Energy Mater.*, 2021, **11**, 2003239.

15 C. Laberty-Robert, K. Valle, F. Pereira and C. Sanchez, *Chem. Soc. Rev.*, 2011, **40**, 961–1005.

16 O. Z. Sharaf and M. F. Orhan, *Renewable Sustainable Energy Rev.*, 2014, **32**, 810–853.

17 A. A. Łatoszyńska, P.-L. Taberna, P. Simon and W. Wieczorek, *Electrochim. Acta*, 2017, **242**, 31–37.

18 T. Norby, *Solid State Ionics*, 1999, **125**, 1–11.

19 K. Kreuer, S. Paddison, E. Spohr and M. Schuster, *Chem. Rev.*, 2004, **104**, 4637–4678.

20 Z. Xue, D. He and X. Xie, *J. Mater. Chem. A*, 2015, **3**, 19218–19253.

21 Z. Zheng, L. Liu, M. Li, W. Sun, Y. Liang, J. Chen, J. Yang, R. Zhang and P. Yin, *J. Phys. Chem. Lett.*, 2023, **14**, 5966–5974.

22 Z. Zheng, Q. Zhou, M. Li and P. Yin, *Chem. Sci.*, 2019, **10**, 7333–7339.

23 S. S. Park, Y. Tulchinsky and M. Dinca, *J. Am. Chem. Soc.*, 2017, **139**, 13260–13263.

24 L. Liu, Z. Wu, Z. Zheng, Q. Zhou, K. Chen and P. Yin, *Chin. Chem. Lett.*, 2022, **33**, 4326–4330.

25 M. M. Rahman, S. Mateti, Q. Cai, I. Sultana, Y. Fan, X. Wang, C. Hou and Y. Chen, *Energy Storage Mater.*, 2019, **19**, 352–359.

26 J. Duan, X. Tang, H. Dai, Y. Yang, W. Wu, X. Wei and Y. Huang, *Electrochem. Energy Rev.*, 2019, **3**, 1–42.

27 S. Y. Kim, S. Kim and M. J. Park, *Nat. Commun.*, 2010, **1**, 88.

28 Q. Li, R. He, J. Gao, J. Jensen and N. Bjerrum, *J. Electrochem. Soc.*, 2003, **150**, A1599–A1605.

29 X.-M. Li, L.-Z. Dong, J. Liu, W.-X. Ji, S.-L. Li and Y.-Q. Lan, *Chem*, 2020, **6**, 2272–2282.

30 S. Srivastava, J. L. Schaefer, Z. Yang, Z. Tu and L. A. Archer, *Adv. Mater.*, 2014, **26**, 201–234.

31 J. A. S. Oh, L. He, B. Chua, K. Zeng and L. Lu, *Energy Storage Mater.*, 2021, **34**, 28–44.

32 X. Miao, H. Wang, R. Sun, C. Wang, Z. Zhang, Z. Li and L. Yin, *Energy Environ. Sci.*, 2020, **13**, 3780–3822.

33 Y. N. Sun, G. R. Gao, G. L. Du, Y. J. Cheng and J. Fu, *ACS Macro Lett.*, 2014, **3**, 496–500.

34 L. Ma, Z. Xu, Y. Chen, M. Zhang, J. Yin, M. Li, K. Chen and P. Yin, *ACS Appl. Mater. Interfaces*, 2020, **12**, 38655–38661.

35 L. Ma, J. Xie, X. Yan, Z. Fan, H. Li, L. Lu, L. Chen, Y. Xin and P. Yin, *Chin. Chem. Lett.*, 2022, **33**, 3241–3244.

36 A. Huang, C. Dong, Y. Gao, L. Liu, X. Yan and P. Yin, *Polymer*, 2024, **299**, 126951.

37 L. Liu, L. Cai, H. Xiao, Y. Lai, Y. Liu, X. Zhou, J. Yin, J. Yang, K. Chen and P. Yin, *Nano Lett.*, 2023, **23**, 2669–2676.

38 P. Yin, D. Li and T. Liu, *Isr. J. Chem.*, 2011, **51**, 191–204.

39 P. Yin, B. Wu, T. Li, P. V. Bonnesen, K. Hong, S. Seifert, L. Porcar, C. Do and J. K. Keum, *J. Am. Chem. Soc.*, 2016, **138**, 10623–10629.

40 Y. F. Song and R. Tsunashima, *Chem. Soc. Rev.*, 2012, **41**, 7384–7402.

41 Z. Zheng, M. Li, Y. Lai, Y. Cao and P. Yin, *Macromol. Rapid Commun.*, 2023, **44**, 2200227.

© 2025 The Author(s). Published by the Royal Society of Chemistry

RSC Appl. Polym., 2025, **3**, 1177–1182 | 1181

42 L. Liu, A. Huang, J. Yang, J. Chen, K. Fu, W. Sun, J. Deng, J. F. Yin and P. Yin, *Angew. Chem., Int. Ed.*, 2024, **63**, e202318355.

43 Z. Zheng, M. Li, Q. Zhou, L. Cai, J.-F. Yin, Y. Cao and P. Yin, *ACS Appl. Nano Mater.*, 2021, **4**, 811–819.

44 L. Liu, Y. Gao, C. Dong, J. Yang and P. Yin, *Chem. – Eur. J.*, 2024, **30**, e202402262.

45 J.-X. Liu, X.-B. Zhang, Y.-L. Li, S.-L. Huang and G.-Y. Yang, *Coord. Chem. Rev.*, 2020, **414**, 213260.

46 T. Hou, W. Xu, X. Pei, L. Jiang, O. M. Yaghi and K. A. Persson, *J. Am. Chem. Soc.*, 2022, **144**, 13446–13450.

47 J. Song, Y. Xiao, L. Zhang, J. Xiang, N. Tang, P. Cheng, J. Zhang, S. Wang and W. Du, *Int. J. Hydrogen Energy*, 2021, **46**, 28246–28257.

48 K. H. Lim, A. S. Lee, V. Atanasov, J. Kerres, E. J. Park, S. Adhikari, S. Maurya, L. D. Manriquez, J. Jung, C. Fujimoto, I. Matanovic, J. Jankovic, Z. Hu, H. Jia and Y. S. Kim, *Nat. Energy*, 2022, **7**, 248–259.

49 K.-S. Lee, J. S. Spendelow, Y.-K. Choe, C. Fujimoto and Y. S. Kim, *Nat. Energy*, 2016, **1**, 16120.

50 S. Wang, X. Li, T. Cheng, Y. Liu, Q. Li, M. Bai, X. Liu, H. Geng, W.-Y. Lai and W. Huang, *J. Mater. Chem. A*, 2022, **10**, 8761–8771.